An Application of the Flow360 Solver to the Hover Download Prediction Problem

Thomas Fitzgibbon*, Charles Doolittle†, Philippe Spalart‡
Flexcompute Inc, Belmont, Massachusetts, 02138

Qiqi Wang§
Flexcompute Inc, Belmont, Massachusetts, 02138
Massachusetts Institute of Technology, Cambridge, Massachusetts 02139

This paper presents the contribution of Flexcompute to the Hover Prediction Workshop, with a focus on hover performance and download predictions. The analysis is focused on HVAB rotor blade simulations at two blade tip Mach numbers of 0.58 and 0.65. First, a rigorous mesh refinement and time step study is performed to assess the discretization error sensitivities for both isolated and installed rotors. The impact of mesh resolution and time step on the performance, sectional loading and flow features is presented with recommendations put forward for engineering level accuracy and high-fidelity solutions. An analysis of loads convergence is also performed, which was found to affect the predictions for installed rotor calculations. Next, a collective sweep study is performed at two blade tip Mach numbers for isolated and installed rotors, and where available comparisons are made with experimental data and predictions from other CFD codes. The Flow360 results showed strong correlation with reference data and resolved high-resolution wake structures, showing the applicability of Flow360 to hovering rotor solutions.

I. Introduction

Hovering rotor predictions are still a major challenge for CFD codes, despite engineering level calculations reaching a high degree of maturity. Many CFD predictions are able to reach an accuracy level of within one count (0.01) in Figure of Merit (FoM) [1–3], however it is still to be determined whether the correct answer is obtained for the correct reasons. Furthermore, a 0.5% error in the FoM prediction is equivalent to the weight of a single passenger [2]. Current experimental datasets only provide a level of accuracy within 1-2 counts in FoM (for example the PSP experimental data in [4]), hence further improvements are required in both computation and experiment.

The hover prediction workshop (HPW) [5] has attempted to improve the accuracy and fidelity hovering rotor simulations, since 2014, and published a status paper in 2017 [6], highlighting many of the outstanding issues. However, many of the points raised are still present in current simulations, especially for more complex problems than for an isolated rotor, and indicate that many hover performance predictions may have good agreement with experimental data due to error cancellation. Although a few highly-resolved solutions exist in literature [1, 2], the majority of studies present underesolved flowfields without rigorous sensitivity studies. If improvements in accuracy of under 0.01 counts in FoM are sought for, understanding the solution sensitivities will be crucial, especially across multiple CFD codes. Rigorous sensitivity studies, however, are difficult for hovering rotors due to high computational costs and long convergence cycles. Another reason is the lack of a comprehensive experimental dataset which could highlight which elements of a hovering rotor flowfield are well captured and which could be improved. The upcoming HVAB blade experimental data from the NFAC facility [7] should facilitate more detailed comparisons and analysis that go beyond integrated loads.

The hover prediction workshop (HPW) has set a new hover focus problem [8], with future research focus on download predictions and in-ground effect simulations of the HVAB rotor. Since this is the first entry to the Hover Prediction Workshop using Flow360, the current paper focuses on the 1^{st} step which includes isolated and installed out-of-ground effect HVAB rotor simulations. While some attempts have been made for isolated rotors in terms of grid

*CFD Research Scientist
†Application Engineer
‡Head of Fluid Mechanics
§Associate Professor, Department of Aeronautics and Astronautics, MIT. Co-founder of Flexcompute

resolution, temporal accuracy and turbulence modelling [2, 9, 10], close to no sensitivity studies exist for installed rotor predictions. For this reason, one of the main aims of the paper is to perform rigorous mesh refinement and time step studies to give higher confidence in the performance predictions for both isolated and installed rotor configurations. Based on the findings from this study a collective sweep is performed for the HVAB blade. Additionally, as the HVAB blade experimental data has not yet been published, lower blade tip Mach number simulations are also performed representative of the PSP blade simulations.

Firstly, the rotor test case for this study is presented, including the geometry and test conditions. Following this, computational modelling aspects are discussed that include the CFD solver, mesh generation and the computational setup. The results section consists of two sections: the first part of the results analyses the mesh refinement and temporal accuracy sensitivities for both isolated and installed rotor simulations; the second part, presents collective sweep results at two blade tip Mach numbers and the results are compared with other CFD codes and available experimental data. Finally, conclusions are drawn along with suggestions for future work.

II. Geometry and Test Conditions

The geometry used for this study is the 4-bladed HVAB rotor, which is the main focus of the Hover Prediction Workshop due upcoming experimental data from the NFAC facility. The IGS file on the hover prediction workshop file share site [11] was used in our simulations. The geometry is highly similar to the PSP rotor blade [12] and features a planform with 14 degrees linear twist, RC-series airfoils and a swept-tapered tip (30 degrees sweep, 0.6 taper ratio outboard of 0.95 radius). The radius of the blade is 66.5 inches with a reference chord (c_{ref}) of 5.45 inches giving a rotor solidity of 0.1033. The flap hinge is located at 3.5 inches with the lag hinge assumed to be coincident. The full rotor blade planform is shown in Figure 1.

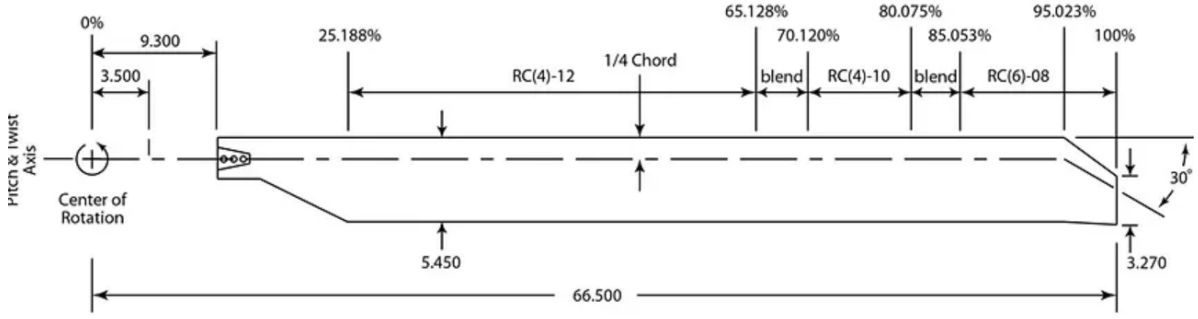

Fig. 1 Geometry of the HVAB rotor blade planform [12].

The HVAB rotor operates at a blade tip Mach number of 0.65 equivalent to 1250 RPM at sea-level standard atmospheric conditions. As aeroelastic effects are not included within the simulations, the cone (β) and lag (ζ) angles are calculated using the following expressions available on the hover focus problem website [8]:

$$\beta = 0.0056\theta_{75}^2 + 0.1139\theta_{75} - 0.6094 \tag{1}$$

$$\zeta = 0.0314\theta_{75}^2 + 0.1299\theta_{75} + 1.5425 \tag{2}$$

Note that the expressions for coning and lag angles, lead to slightly different values than those provided in [12] across the range of collective angles. As the HVAB rotor blade is highly similar to the PSP rotor blade, the same geometry is used for representative PSP rotor blade simulations. Only the Mach number is changed, as the PSP rotor blade operates at a blade tip Mach number of 0.58. The primary differences between the two geometries are a different shape inboard of 25% radius, as the HVAB blade includes the instrumentation cuff) and higher trailing edge thickness of the HVAB blade (0.035 inches compared to 0.03 inches for the PSP blade). Another difference is the different location of the flap hinge which is located at 3 inches for the PSP blade, as well as different structural properties, which would lead to different flap/lag angles. Despite this, the impact on the integrated loads is likely to be minimal as the dynamic head near the root is low in hovering rotor conditions and the impact of coning is low on the FoM values [13]. Calculations are performed across a range of collective angles (θ_{75}) from 6 to 11 degrees.

For installed rotor calculations, the NASA Robin-mod7 fuselage is used as recommended by the hover focus problem [8]. This generic fuselage has an analytical definition with the cross sections defined by a series of superellipses. The superellipse coefficients were obtained from [14]. The fuselage geometry was generated in Engineering Sketch Pad (ESP) [15] using 45 cross sections and compared visually to the Plot3D geometry available on the hover prediction workshop file share site [11]. The geometry does not include the main rotor pylon or the rotor hub. The fuselage has a length of 123.931 inches and was pitched up by 3.5 degrees. The offsets of the fuselage nose from the rotor center were taken from [8] (the rotor was positioned at (0,0,0) with the offsets equal to (-42.78, 0.0, -24.98)). The full configuration of the HVAB blades (at 10 degrees collective) with the fuselage is shown in Figure 2.

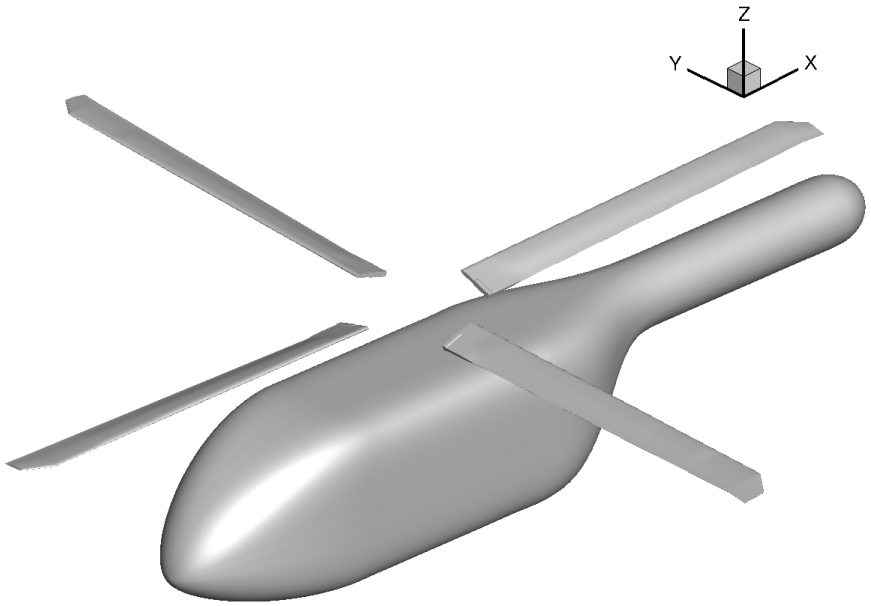

Fig. 2 Geometry of the Robin-mod7 fuselage with the HVAB rotor blades pitched at 10 degrees collective.

III. Computational Modelling

The following section introduces the Flow360 solver and the computational methodology used for hovering rotor calculations. Following, the process of mesh generation is analyzed focusing on the choices made for the mesh refinement study.

A. Flow360 CFD Solver

Flow360 is based on hardware/software co-design with emerging hardware computing leading to unprecedented solver speed without sacrificing accuracy. The Flow360 solver is a node-centered unstructured grid solver based on a 2nd order finite volume method. The convective fluxes are discretized using the Roe Riemann solver, whereas central differences are used for the viscous fluxes. MUSCL extrapolation is used to achieve higher order accuracy in space. Flow360 includes a number of standard turbulence models including SA-neg, SA-RC, $k-\omega$ SST, and DDES. Transition modelling capabilities are also available based on the 3-equation SA-AFT model, but are not used in the present work. All simulations within this paper are performed as time-accurate using the dual time-stepping technique with the time derivative discretized using an implicit second-order accurate backward Euler scheme.

B. Computational Setup

The Flow360 solver uses the sliding interface methodology to model relative motion of individual components. The domain in split into a nearfield rotating block which encloses the rotor blades and a farfield stationary block which contains the fuselage in the case of installed rotor cases. Data is interpolated between the two blocks using a 2nd order scheme. To minimize the computational costs, strict constraints are imposed on the node layout on the sliding interface, as all nodes must lie on concentric circles, as shown in Figure 3.

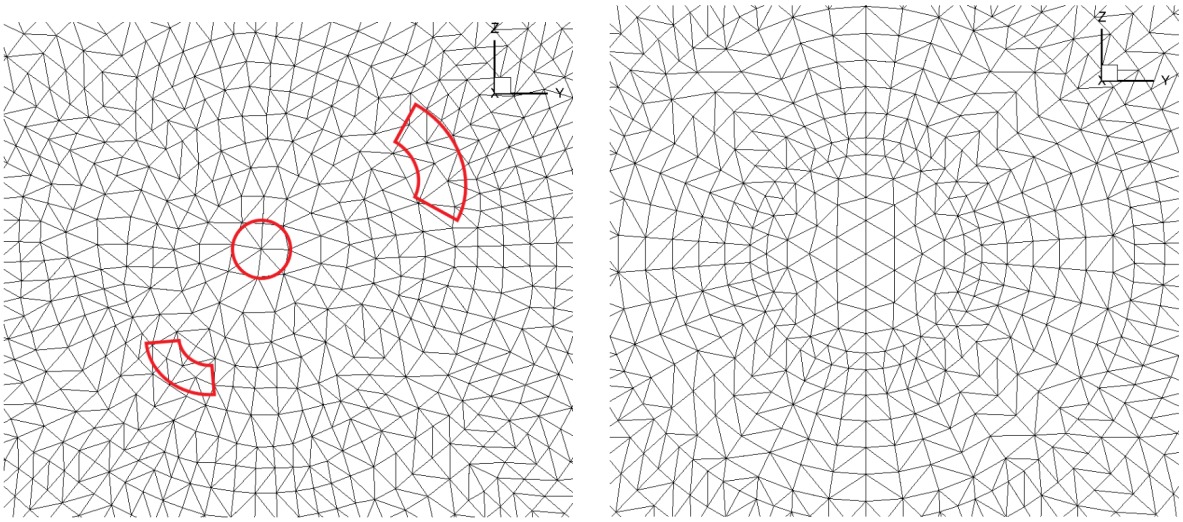

(a) Invalid (b) Valid

Fig. 3 Requirements for distribution of nodes on the sliding interface.

As can be seen Figure 3 a) does not meet the concentricity requirements as many of the nodes do not lie on concentric circles. Figure 3 b) meets this requirement. This leads to a significant reduction in computational overhead as no interpolation weights need to be calculated or stored as the position of each node is known at every time step. As mentioned previously, aeroelastic effects are not modelled, with the blade treated as rigid with imposed collective, coning and lag angles. The SA-RC-DDES turbulence model is used throughout this study. The primary reason for this is an overprediction of the turbulent eddy viscosity ratio levels in the rotor wake for RANS-based models [16, 17], typically leading to an overprediction of the rotor torque. This is also one of the limitations of simulations performed using the steady-state hover formulation which are typically RANS-based. All the calculations in this study are performed using the unsteady solver. The CFL number is ramped up from 1 to 1e6 over 30 linear iterations within each time step, with 35 linear iterations used in total. The flow is first initialized using a 1st order solver for one revolution with a 6 degree time step. Then 18 to 24 revolutions are computed using the 2nd order solver using the same 6 degree time step, with the main purpose to establish the wake and advect the starting vortex. This procedure is similar to simulations with a low time step (of 0.25 degrees for example) and low number of linear iterations within each time step as used in [18]. The high possible time-step highlights the robustness of the Flow360 solver. Following this, the simulation is continued using a lower time-step. In the case of the time-step study, 6 revolutions are computed using a 3 degree time step followed by another 6 revolutions using 1 degree time step and 6 revolutions using a 0.5 degree time step. For the installed rotor cases, an additional 6 to 8 revolutions are computed using a 0.25 degree time step. In the case of the collective sweep simulations, the simulations are continued after the initial start-up (6 degree time step), using the final time step value for an additional 6 revolutions. The number of revolutions was based on the loads convergence and establishment of periodicity. It should, however, be noted that the installed rotor calculations included long transients in the loading components potentially requiring a higher number of revolutions for statistical convergence. For this reason, error bars are included in the integrated load results, which are computed by splitting the loading signal into samples (1 sample per revolution) and computing the standard error of the sample means based on a 95% confidence interval. The final loading results are averaged over the 5 revolutions, leading to 5 samples in the confidence interval computation, meaning that the confidence interval is of the same order of magnitude as the standard deviation due to the low sample size (factor of 0.8765). The error bars for FoM and Download are computed by taking the maximum and minimum possible values, taking into account the accumulation of errors in rotor thrust/torque and fuselage thrust

values. Regarding, residual convergence, the solver moves to the next time-step once 2 orders of residual magnitude reduction are achieved. The convergence is worsened as the grid is refined and the collective angle is increased, but improved with time step reduction. For the majority of cases, at a time step of 6 degrees, 1.5 orders of magnitude are achieved for all residuals for the finest grid, whereas 2 orders of magnitude are achieved before completing the full number of linear iterations at the lowest examined time steps of 0.5 degree for the isolated rotor and 0.25 degree for the installed rotor. The mesh refinement and time-step studies are performed at a collective angle of 10^o. For the collective sweep, angles of 6^o, 8^o, 9^o, 10^o and 11^o are computed at two blade tip Mach numbers of 0.58 and 0.65.

C. Mesh Generation

All meshes within this work were generated using Pointwise V18.6R1 [19]. The automated surface meshing tool, Flashpoint, was used to generate the surface meshes with the unstructured 3D solver with TRex (anisotropic meshing tool) for the volume meshes. As a sliding interface method was used to model the rotor rotation, and currently, Flow360 does not have mesh deformation capabilities, the meshes were regenerated for each collective angle and mesh refinement level. Therefore, the pitch, flap and lag angles were imposed on the geometry through a series of translations (to account for flap/lag center offset) and rotations. For the mesh resolution study, five mesh levels were generated based on the reference chord length (c_{ref} of 5.45 inches). The values used are: 20% c_{ref}, 15% c_{ref}, 10% c_{ref}, 7.5% c_{ref} and 5% c_{ref}. For the surface mesh the maximum edge length was set to 0.545 for the 10% c_{ref} mesh and the refinement factor value was used to generate the other meshes. The resolution at the leading edge, trailing edge and blade tip was primarily controlled by the curvature resolution parameter which was set to 5 degrees. Therefore, the spacing at the leading and trailing edges was not explicitly defined. The quad dominant algorithm was used, with anisotropic layers growing from the leading and trailing edges until isotropy is reached. A boundary growth of 1.2 and maximum aspect ratio of 400 was used for all surface meshes. Difficulties were encountered in meshing the transition between the blunt trailing edge in the main portion of the blade and the thick portion near the root, as the Flashpoint parameters had to be iteratively adjusted to ensure sufficient mesh quality. The number of nodes across the blunt trailing edge was enforced for each mesh, while the faces on the trailing edge in the root portion of the blade were handled using the Flashpoint solver, which led to the over resolution of this region, but ensured good surface/volume mesh quality. Similarly, Flashpoint was also used for the fuselage meshes, with the same maximum spacing as on the blades and 5 degree curvature resolution angle. The fuselage surface meshes are tet-dominant. Example 20% c_{ref}, 10% c_{ref} and 5% c_{ref} rotor blade surface meshes are shown in Figure 4, with the surface mesh parameters and statistics shown in Table 1.

Table 1 Surface mesh statistics for the mesh resolution study. ΔS = spacing, N = number of nodes, ΔA = area ratio, AR = aspect ratio

Target ΔS	TE N	Max ΔS	Max ΔA	Max AR	LE ΔS	TE ΔS	N (blade)	N (fus.)
20% c_{ref}	7	22.4%c_{ref}	7.029	251.9	0.0035 c_{ref}	0.00071 c_{ref}	19487	8920
15% c_{ref}	8	18.8%c_{ref}	6.709	282.8	0.0027 c_{ref}	0.00051 c_{ref}	33120	12782
10% c_{ref}	12	13.3%c_{ref}	5.973	280.4	0.0018 c_{ref}	0.00035 c_{ref}	69600	28609
7.5% c_{ref}	17	9.47%c_{ref}	6.005	318.8	0.0014 c_{ref}	0.00023 c_{ref}	123123	52378
5% c_{ref}	25	6.7%c_{ref}	5.491	350.3	0.00094 c_{ref}	0.000153 c_{ref}	258645	120240

For the volume meshes, as mentioned previously the domain is split into a rotating nearfield block and a farfield stationary block. The sliding interface was placed from -0.075R to 0.105R (-5 inches to +7 inches), where R is the rotor radius of 66.5 inches. This ensured that enough spacing is left between the sliding interface and fuselage surface to allow anisotropic layers to grow on the fuselage surface, but also that the interface is far enough from the blade surface. The sliding interface is not centered around 0, as the blades are coned. The wall spacing is set to 3.67e-06 c_{ref} (2e-05 inches), which on both the blades and the fuselage, which ensures a y^+<1 on the surfaces. Anisotropic layers are grown from the solid surfaces with the growth rate depending on the mesh refinement level, until isotropy is reached. This means that hexahedral elements are present in the blade boundary layers and prism elements in the fuselage boundary layer which both transition to a tetrahedral mesh in the farfield. To resolve the wake, three levels of refinement are used. The first level is set to the same spacing as the maximum edge length on the surface and is placed from the top of the sliding interface at 0.105R to -2R which is the location where the top surface of the fuselage is located in the installed rotor cases. The second level is coarser by a factor of 2 and is placed from 0.4R to -0.9R. The third level again coarsens

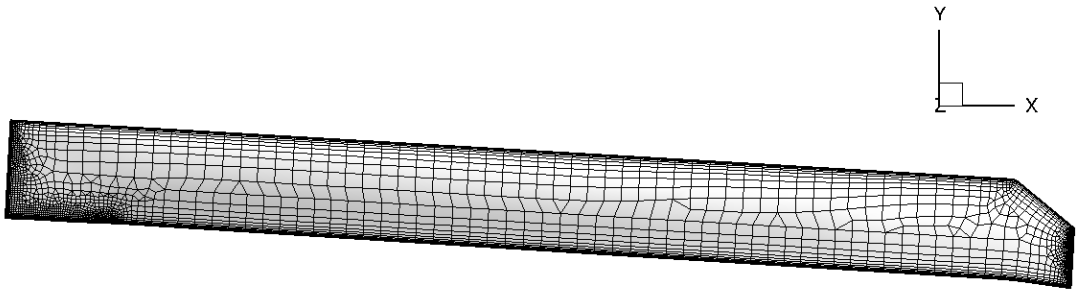

(a) 20% c_{ref}

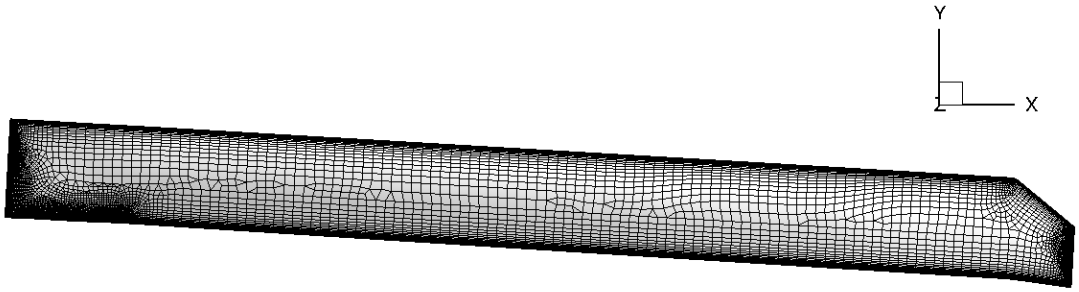

(b) 10% c_{ref}

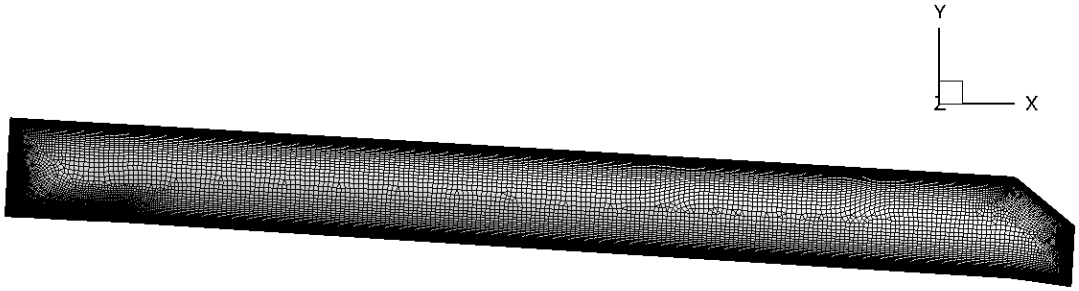

(c) 5% c_{ref}

Fig. 4 Surface meshes for three of five levels (20% c_{ref}, 10% c_{ref}, 5% c_{ref}) used for the mesh refinement study.

by a factor of 2 and is placed from 0.6R to -1.8R. As the primary focus is on integrated loads prediction, the refinement is not extended further downstream. The upstream refinement is there to ensure that the mesh transitions smoothly and that the inflow velocity gradient is well-resolved. The farfield is placed at 50R away from the center of rotation. An example slice through the volume mesh at y=0 is shown in Figure 5 for the 10% c_{ref} mesh with the fuselage. Note that the blades cannot be fully seen here, as the blades are lagged. The volume mesh parameters and statistics are shown in Table 2.

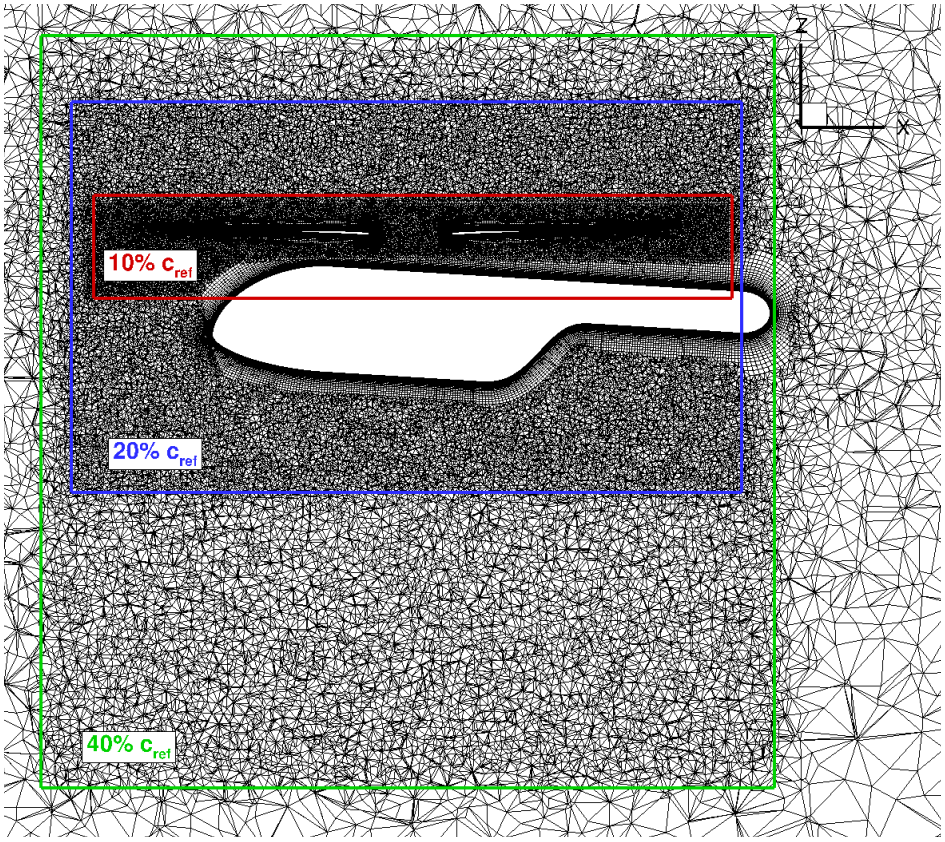

Fig. 5 Slice through $y = 0$ of the 10% c_{ref} volume mesh for the installed rotor case at 10^o collective, highlighting the mesh refinement regions.

Table 2 Volume mesh statistics for the mesh resolution study. ΔS = spacing, W. GR = Wall Growth Rate, Ref. = Refinement, N = number of nodes, Near. = Nearfield, Far = Farfield, Far Fus. = Farfield with Fuselage, iso = isolated, ins = installed.

Target ΔS	W. GR	Ref. 1	Ref. 2	Ref 3.	N Near.	N. Far	N (iso)	N. Far Fus.	N (ins)
20% c_{ref}	1.25	20% c_{ref}	40% c_{ref}	80% c_{ref}	3.3M	0.3M	3.6M	0.8M	4.0M
15% c_{ref}	1.2	15% c_{ref}	30% c_{ref}	60% c_{ref}	6.4M	0.7M	7.1M	1.4M	7.8M
10% c_{ref}	1.17	10% c_{ref}	20% c_{ref}	40% c_{ref}	15.0M	2.0M	17.0M	4.2M	19.0M
7.5% c_{ref}	1.14	7.5% c_{ref}	15% c_{ref}	30% c_{ref}	30.0M	4.4M	34.4M	8.3M	38.0M
5% c_{ref}	1.11	5% c_{ref}	10% c_{ref}	20% c_{ref}	74.9M	13.9M	88.2M	24.3M	98.6M

IV. Results

This section discusses the results of the current study. Firstly, the mesh refinement and time step study is presented. Following, results are presented from the collective sweep at two blade tip Mach numbers for both isolated and installed rotors. Before presenting the results, the standard definitions for the integrated loads are defined, as well as the sectional loads. The thrust coefficient, torque coefficient and figure of merit (FoM) are defined as follows:

$$C_T = \frac{T}{\pi\rho\Omega^2 R^4}, C_Q = \frac{Q}{\pi\rho\Omega^2 R^5}, FoM = \frac{C_T^{3/2}}{(\sqrt{2}/C_Q)} \tag{3}$$

The sectional loads are normalized by the local chord and the local velocity as follows:

$$C_t = \frac{T_b}{1/2\rho c R^2(\Omega r)^2}, C_q = \frac{Q_b}{1/2\rho c R^3(\Omega r)^2} \tag{4}$$

A. Mesh Refinement and Time Step Studies

1. Isolated Rotor

The integrated loads convergence for the isolated rotor with a mesh refinement and time step is shown in Figure 10. The integrated loads are plotted versus grid factor where N is the number of mesh nodes for the mesh refinement study.

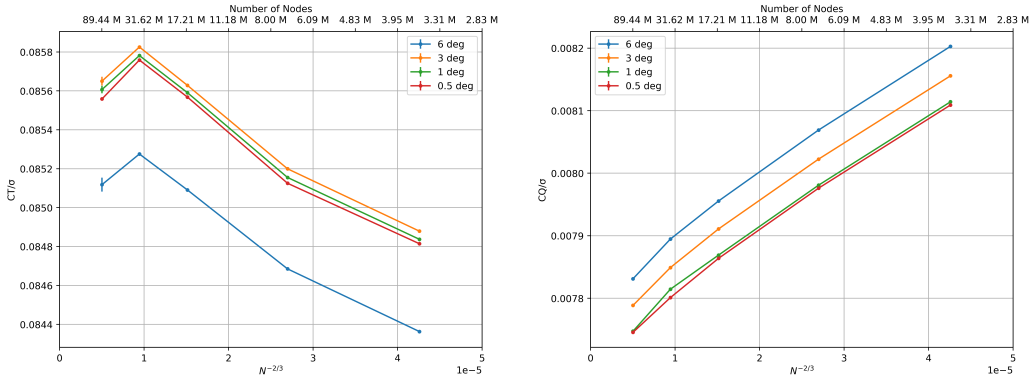

(a) C_T/σ vs $N^{-2/3}$ (b) C_Q/σ vs $N^{-2/3}$

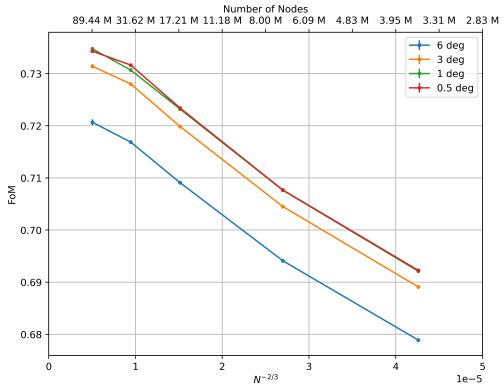

(c) FoM vs $N^{-2/3}$

Fig. 6 Rotor integrated loads convergence with mesh and time step refinement for the isolated HVAB rotor at 10^o collective.

The first aspect that must be highlighted is the close to negligible error bars for the integrated loads for the isolated rotor computations. Of course, the loading signals has a 4/rev dominant component, however, the error bars indicate that the values are well converged. The mesh refinement study, shows that as the mesh is refined generally, the thrust increases and the torque reduces, leading to an increase in the performance of the rotor. This is true for all mesh levels apart from the final mesh, where the rotor thrust convergence with mesh refinement exhibits non-linear behavior, leading to a slight non-linearity in the FoM curve. The torque shows very good convergence properties with mesh refinement and is close to linear. Regarding the time step convergence, the thrust initially goes up with a reduction in time step and then slowly reduces. The difference between the values at 1 degree and 0.5 degree time steps is close to negligible although some non-linearity can be seen for the finest mesh when moving to the finest examined time step. The torque reduces leading to an increase in the FoM values as the time step is refined with very minor differences for the finest two time steps.

To results are examined in further detail to explain the behavior of the integrated loads with mesh refinement and a reduction in time step. A particular focus in put on the non-linearity in the thrust coefficient present for the finest

mesh. To examine the differences, further post-processing is performed for the finest time step across the different mesh refinement levels and for the finest mesh across different time steps. Firstly, the sectional loads are examined, shown in Figure 7.

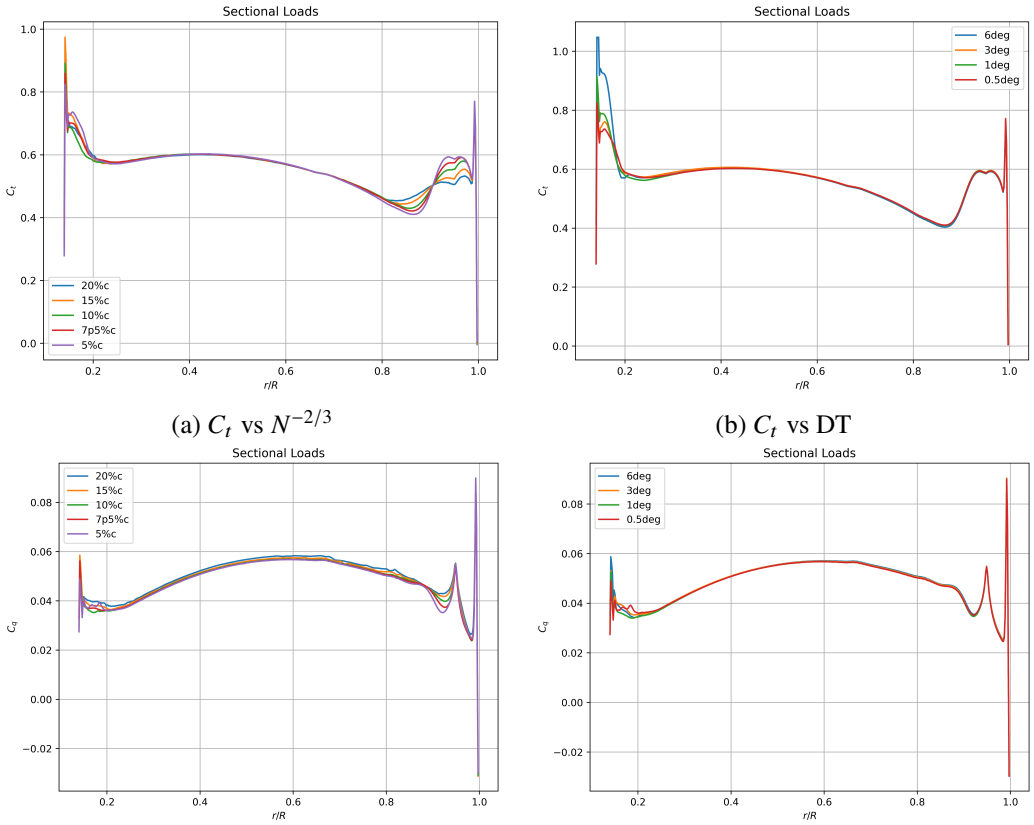

(a) C_t vs $N^{-2/3}$

(b) C_t vs DT

(c) C_q vs $N^{-2/3}$

(d) C_q vs DT

Fig. 7 Sectional loads convergence with mesh and time step refinement for the isolated HVAB rotor at 10^o collective.

The sectional loads show a strong sensitivity to mesh refinement, with only minor changes with a reduction in time step. Refinement of the mesh leads to a significantly better resolved tip vortex has a large impact on the sectional loading inboard and outboard of approximately r/R = 0.9. Inboard, the preceding tip vortex induces downwash leading to a reduction in the local sectional loading, whereas outboard the tip vortex induces upwash leading to an increasing in the local sectional loading. With mesh refinement, the location at which the tip vortex starts to impact the local loading also moves further inboard. An increase in local thrust is also seen outboard of r/R= 0.95 with mesh refinement which is not the case when comparing the 5% and 7.5%c results. There is also a high sensitivity inboards, however, the differences are exacerbated due to scaling with local velocity. The time step primarily impacts the sectional thrust inboard, with the sectional thrust reducing with a reduction in time step. Mesh refinement also leads to a reduction in local torque along the entire blade, especially in the location of the tip vortex. Again, the effect of time step on the sectional torque is fairly low. To examine the differences seen at the blade tip with mesh refinement, the skin friction contours and skin friction lines are presented in Figure 8.

The skin friction lines indicate, that there is still a meshing sensitivity present even for the finest mesh solution. As the mesh is refined a shock starts to appear inboard of the blade tip causing shock induced separation. The separation region over the blade tip, however, increases in the spanwise direction but reduces in size in the chordwise direction with mesh refinement. Further potential improvements could be made to the surface mesh, to ensure that these features are well mesh converged. As the DES turbulence model was used, it was decided to not allow the spanwise spacing to be much larger than the chordwise spacing, however, based on these results, a lower growth rate from the leading edge could be beneficial with a trade-off in increasing the spanwise spacing. Due to the meshing sensitivity on the flow

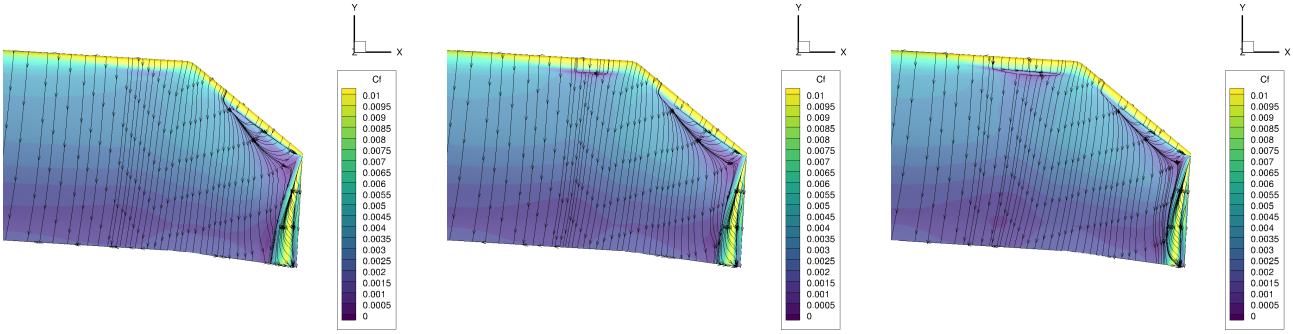

(a) 10%c (b) 7.5%c (c) 5%c

Fig. 8 Skin friction with skin friction lines with mesh refinement for the isolated HVAB rotor at 10^o collective.

features it was decided to proceed forward with the finest mesh for the collective sweep, although the 7.5%c mesh, could still be deemed as an appropriate engineering level accuracy mesh due to the low sensitivity in integrated loads. The time step for the collective sweep was chosen to be 0.5 degrees, to ensure that a robust solution is obtained at other conditions, which may exhibit different mesh convergence and time step sensitivities. Finally, the wakes a visualized using Q-criterion contoured with Mach number, shown in Figure 9.

The wake visualizations show a strong dependency of the mesh on the resolved flow features. The 20%c mesh was not shown here, as it looks highly similar to the 15%c mesh. For the coarsest mesh, the tip vortices are poorly resolved and start to dissipate past the 1st level of mesh refinement. The solution actually highly resembles a blade-element theory solution where only a streamtube is visible. As the mesh is refined the vortices are better resolved, with the 7.5%c resembling a good engineering quality wake resolution. The 5%c mesh shows instabilities in the rotor wake seen in high-fidelity solutions. The secondary structures, which are also seen in other studies [20], are resolved, and are due to the interaction of the tip vortices with the shear layers. The integrated loads also highlighted that an engineering level accuracy solution can be obtained with the 7.5%c grid and higher time step of 1 degree, as the differences with further refinement were low.

2. Installed Rotor

The integrated loads convergence for the installed rotor with a mesh refinement and time step is shown in Figure **??**. The convergence of the total thrust and fuselage download in shown in Figure 11. The integrated loads are plotted versus grid factor where N is the number of mesh nodes for the mesh refinement study.

The first observation that stands out from the integrated loads plots is the much larger error bars on the integrated load predictions. The primary reason for this is the presence of non 4/rev components with long transients in the loads, meaning that further revolutions could be required to obtain tighter error bars. Another aspect is that as the loads were averaged over 5 revolutions with 5 samples used in the confidence interval computation, the error bars are close to plus/minus one standard deviation. The rotor thrust convergence is linear for the coarser meshes, but shows a spectrum values for the finer meshes. The rotor torque convergence with mesh refinement is much better behaved although also shows certain non-linear behavior, particularly for the 7.5%c mesh. Similarly as for the isolated rotor, the rotor thrust generally increases with mesh refinement, apart from the finest level mesh, whereas the torque reduces. The rotor figure of merit value also increases with mesh refinement. All values of FoM fall within 0.5 a count for time steps below 3 degrees and refinement level below 10%c, showing high confidence in the fine mesh/fine time step results. The total thrust and download values show a high degree on non-linearity with mesh refinement, with fairly high error bars. The values for the two finest mesh levels and two finest time levels are, however, within 1.5% in download and 1% in total thrust. The time step study, indicates that time step values such as 6 degree or 3 degrees led to an overprediction of the fuselage download for the finest mesh, and underprediction in FoM. A certain degree of non-linearity is also seen in the time step convergence especially for the finer time steps. Before analyzing the results further, the loading convergence properties are analyzed with a comparison to the isolated rotor convergence for the 5%c mesh and 0.25 degree time step (0.5 degree for isolated). The convergence of the key performance parameters, FoM and fuselage download, for the isolated and installed cases are shown in Figure 12.

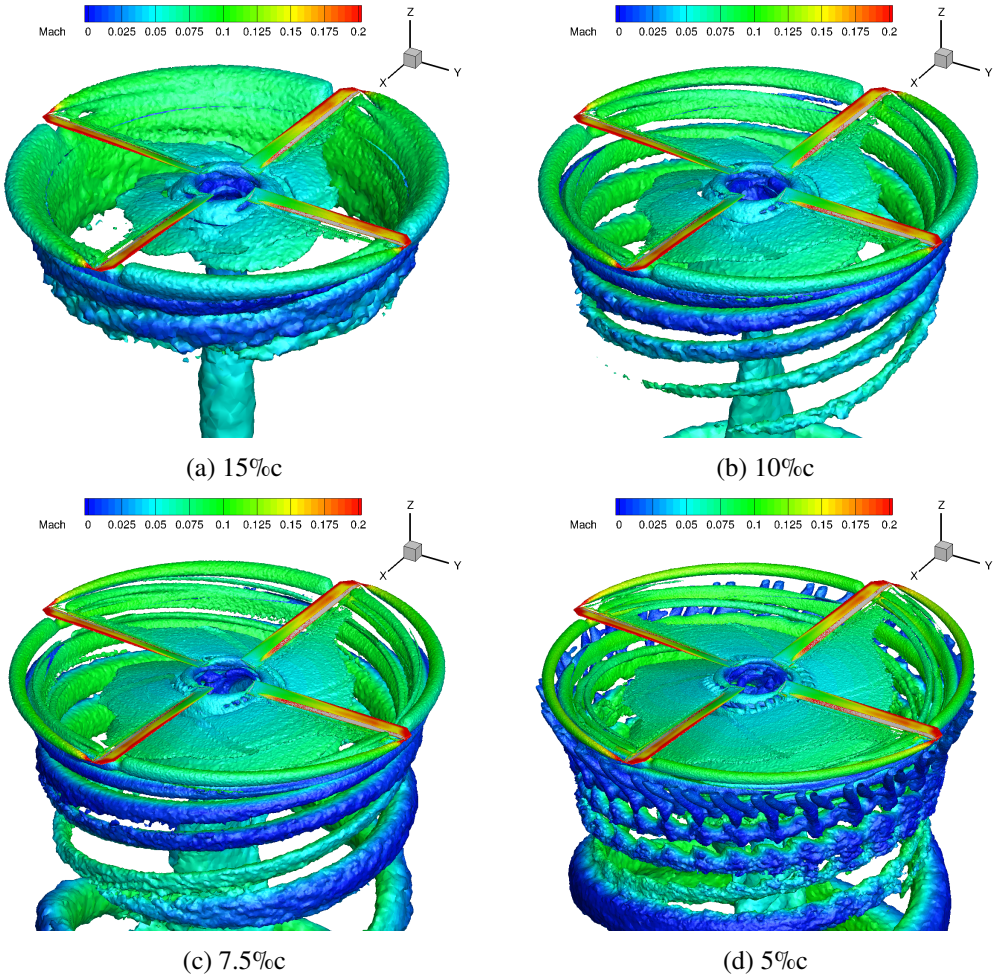

(a) 15%c (b) 10%c

(c) 7.5%c (d) 5%c

Fig. 9 Wake visualization using Q-criterion (2e-06) with mesh refinement for the isolated HVAB rotor at 10^o collective.

As can be seen from the convergence plots, the convergence of the loads is much tighter for the isolated rotor. The FoM variation over the last 3 revolutions is less than 0.2 counts in FoM. For the installed rotor, the convergence histories are shown over 6 revolutions and it can be seen that long transients exist in the installed rotor calculations. The rotor FoM and fuselage download values oscillate slowly over approximately 5 revolutions. The oscillations are in the order of 1 count in FoM and slightly over 1% in fuselage download. The convergence history plots explain the larger error bars for the installed calculations and to reduce these errors, at least 20 revolutions should be simulated to obtain highly accurate integrated loads data. To examine where these long transients come from, the averaged surface pressure on the fuselage is extracted over 4 revolutions, shown in Figure 13.

The surface pressure distributions indicate there are two key regions with highly unsteady loading. The first region is the root region of the blade. As a hub was not modelled, strong root vortices are produced which interact with the fuselage. As the dynamic head is low here, the convergence of these flow features is very slow. The second region is the lower surface of the fuselage behind the fuselage ramp. Here, vortex shedding occurs with a frequency of approximately 0.2/rev based on the loads convergence. This feature is the main reason behind the long transients present in the installed rotor convergence cycles. Another important aspect of note, is that the main portions where download is produced, on the upper surface of the fuselage are well converged, as seen in the low variation in the forward and aft sections of the fuselage. Based on the convergence histories and unsteadiness in fuselage loading, some care has to be taken in interpreting the mesh refinement and time study results, especially when differences are observed in the regions of highly unsteady loading. To examine the differences, further post-processing is performed for the finest time step across

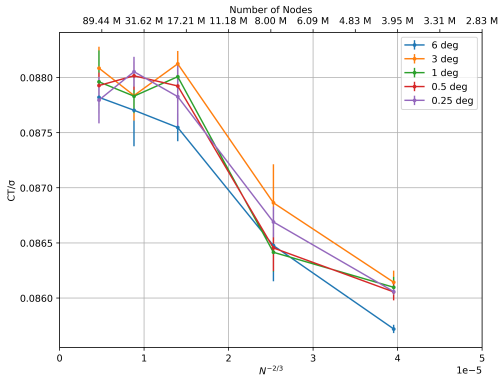

(a) C_T/σ vs $N^{-2/3}$

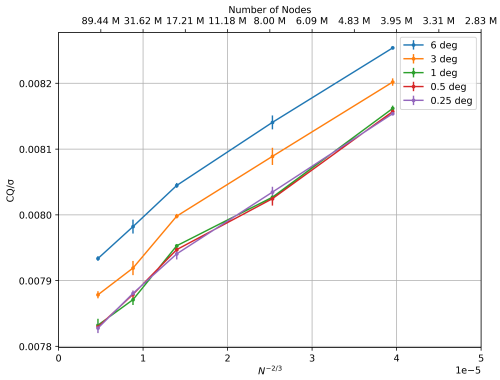

(b) C_Q/σ vs $N^{-2/3}$

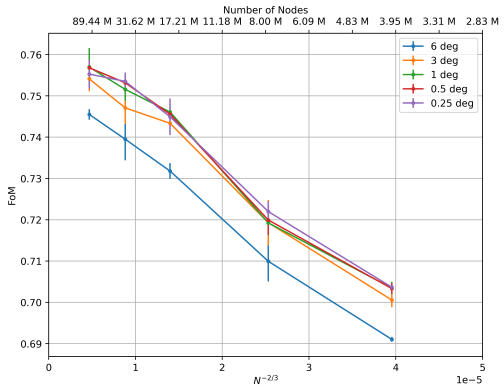

(c) FoM vs $N^{-2/3}$

Fig. 10 Rotor integrated loads convergence with mesh and time step refinement for the installed HVAB rotor at 10^o collective.

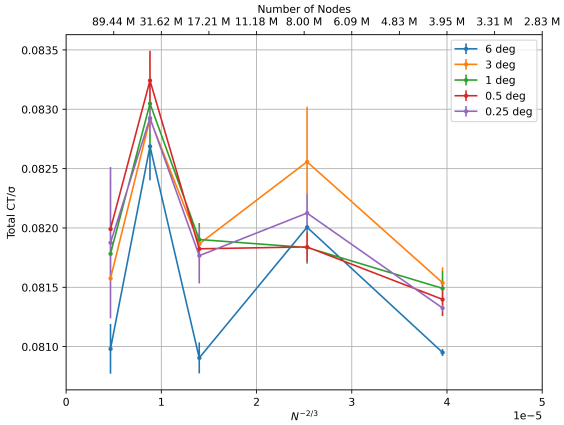

(a) C_T/σ (Total) vs $N^{-2/3}$

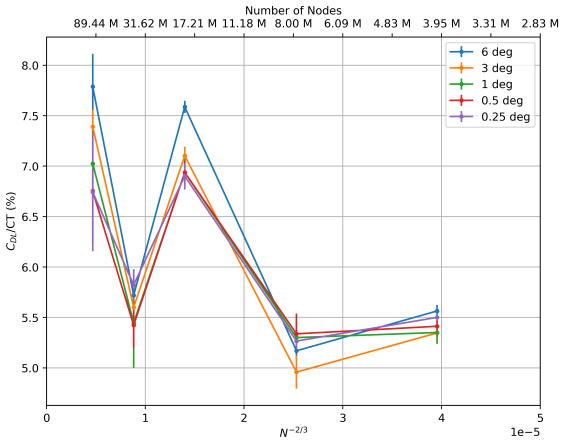

(b) C_{DL}/C_T (%)

Fig. 11 Fuselage download and total system thrust convergence with mesh and time step refinement for the installed HVAB rotor at 10^o collective.

the different mesh refinement levels and for the finest mesh across different time steps. Firstly, the sectional loading convergence is examined at the blades aft ($\psi = 0^o$) and forward ($\psi = 180^o$) shown in Figures 15-14, along with the azimuthally-averaged fuselage surface pressure shown in Figure 16.

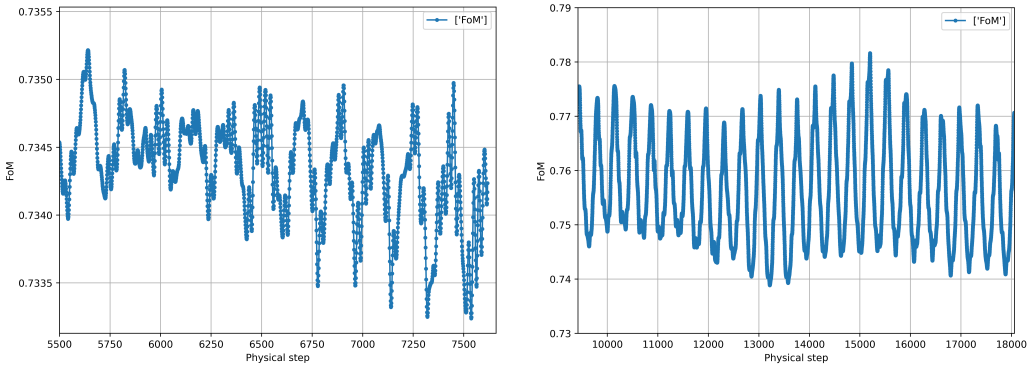

(a) FoM, Isolated Rotor

(b) FoM, Installed Rotor

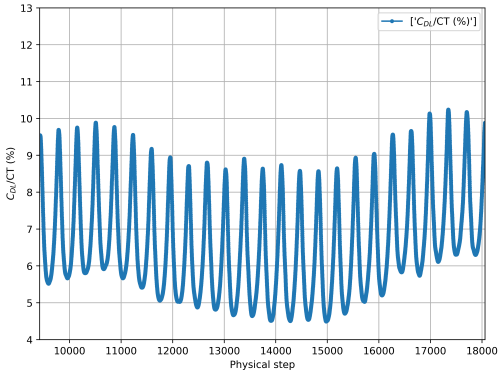

(c) Fuselage Download, Installed Rotor

Fig. 12 Integrated loads convergence for the isolated and installed HVAB rotor cases.

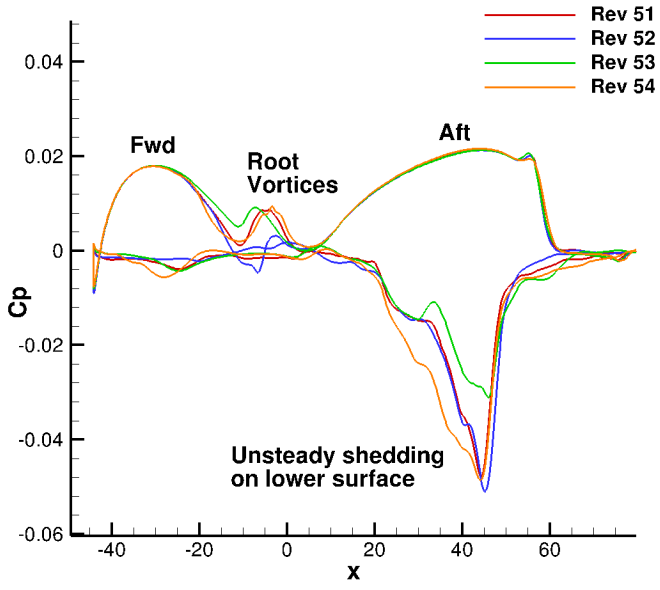

Fig. 13 Surface pressure variation on the fuselage surface over 4 revolutions.

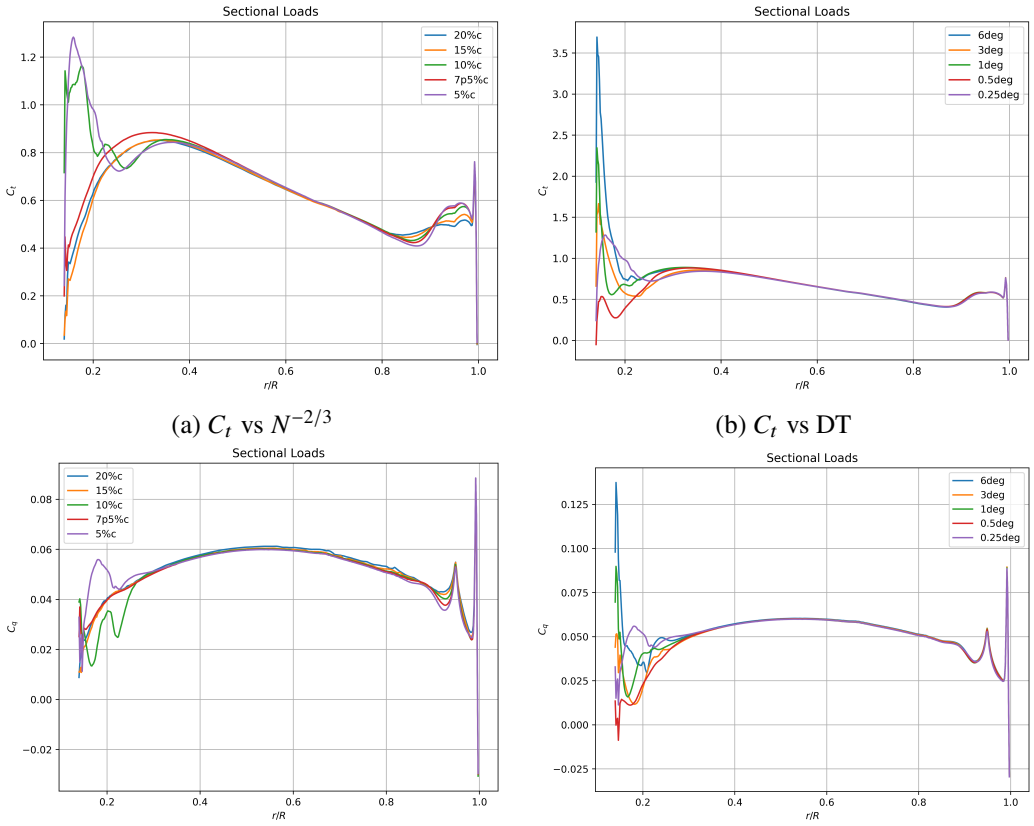

(a) C_t vs $N^{-2/3}$

(b) C_t vs DT

(c) C_q vs $N^{-2/3}$

(d) C_q vs DT

Fig. 14 Sectional loads convergence with mesh and time step refinement for the installed HVAB blade at 10^o collective at $\psi = 180^o$ (fwd).

As the sectional loads are instantaneous a high degree of variability is seen near the root. Once again, however, these differences are exacerbated by the fact that the sectional loads are scaled with the local velocity which is close to zero in the inboard regions. Converging these flow features is, however, difficult, as no hub is present and the strong root vortices induce an upwash inboard. In the outboard locations, similar observations can be made as for the isolated rotor sectional loads. The upwash from the fuselage increasing the loading on the blade at $\psi = 180^o$. The increase in local angle of attack due to the upwash means that as the mesh is refined, the sectional thrust at the blade tip initially goes up but then drops for the finest mesh due to shock induced separation. Similarly as for the isolated rotor, a the largest effect on the sectional loading is due to the better resolved preceding tip vortex. The sectional torque also drops with mesh refinement. The time step does not appear to have a large impact on the sectional loads for the forward blade. The sensitivity of both mesh and time step is much higher on the aft blade at $\psi = 0^o$. Here, a sensitivity can be found not only at the very root but also slightly further outboard up to r/R = 0.4. The 7.5%c mesh seems to behave differently than the 10%c and 5%c meshes, which is the main contributor between the non-linear convergence in the total thrust and fuselage download. The sectional thrust also varies non-linearly here with time step although the differences are reduced. The torque coefficient distributions follow similar trends as the sectional thrust. The fuselage surface pressure, further highlights the non-linearity in the sectional loads on the aft blade, with the 7.5%c mesh predicting a lower download. The areas of unsteadiness highlighted previously, also appear here to be not mesh converged with also a large sensitivity to time step. These regions, however, highlight that an averaging over a much longer cycle is required. The fuselage surface pressure, however, highlights that the download due to the aft blade passage is much more mesh and time step sensitive than the forward portion. Finally, similarly as for the isolated rotor the wakes are visualized using Q-criterion shown in Figure 17.

Similar observations can be made as for the isolated rotor, although some additional structures are present beneath the fuselage as well as at the fuselage tail. The root flow is also less settled compared to the isolated rotor due to

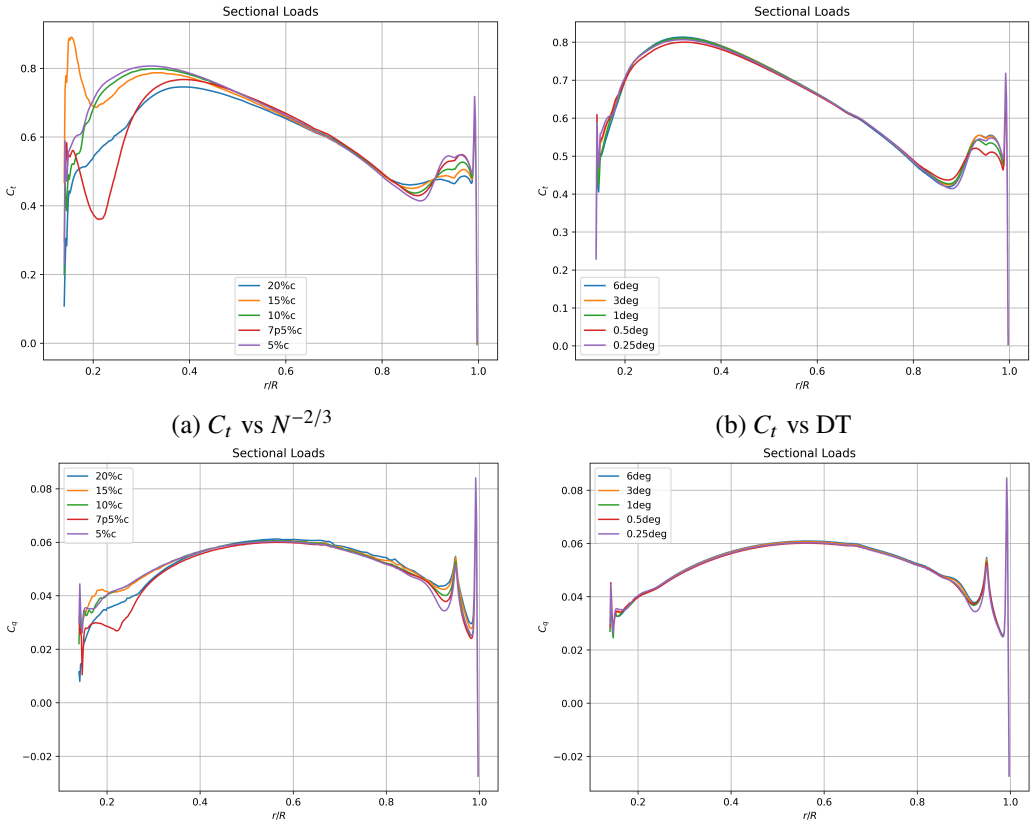

(a) C_t vs $N^{-2/3}$

(b) C_t vs DT

(c) C_q vs $N^{-2/3}$

(d) C_q vs DT

Fig. 15 Sectional loads convergence with mesh and time step refinement for the installed HVAB blade at 10^o collective at $\psi = 0^o$ (aft).

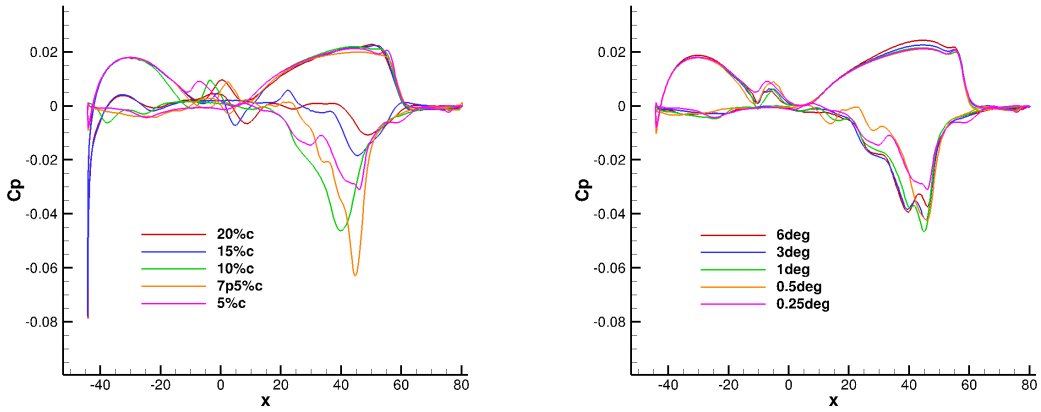

(a) C_p vs $N^{-2/3}$

(b) C_p vs DT

Fig. 16 Azimuthally-averaged fuselage surface pressure convergence with mesh and time step refinement for the installed HVAB blade at 10^o collective.

the presence of the fuselage. Similarly as for the isolated rotor, the finest mesh and finest time step is chosen for the collective sweep study to ensure high robustness of the obtained results.

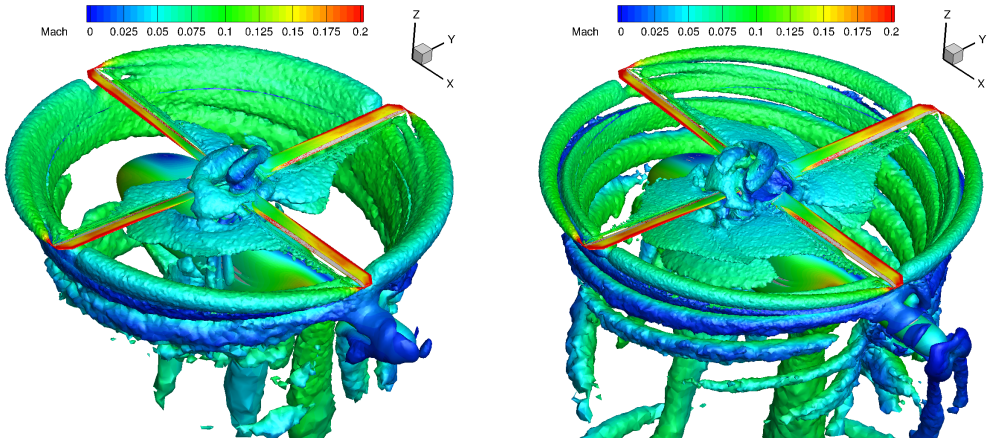

(a) 15%c (b) 10%c

(c) 7.5%c (d) 5%c

Fig. 17 Wake visualization using Q-criterion (2e-06) with mesh refinement for the installed HVAB rotor at 10^o collective.

B. Collective sweep study

The collective sweep study is performed next, for the 5%c mesh using time steps of 0.5 degree for the isolated rotor and 0.25 degree for the installed rotor. The study is performed at two blade tip Mach numbers 0.58 and 0.65 for additional comparisons with other CFD codes and experimental data. The isolated rotor results are presented first, followed by the installed rotor results.

1. PSP representative results - $M_{tip} = 0.58$

The integrated loads for both isolated and installed rotors at $M_{tip} = 0.58$ are presented first, representative of the PSP rotor results, shown in Figure 18. The Flow360 predictions are compared with experimental data and data from other CFD simulations. The experimental data was taken from Overmeyer and Martin [4], whereas the CFD predictions can be found in the following references: Helios/OVERFLOW [1], HMB3 [21], Helios/FUN3D [22].

The hover performance predictions in terms of FoM from Flow360 show good agreement with experimental data and a number of CFD codes. As stated by Overmeyer [4], the fully turbulent approximation should follow the fixed lower surface data at loadings above $C_T/\sigma = 0.7$ as the upper surface naturally becomes turbulent, whereas the fixed upper/lower surface data is more applicable at loadings below $C_T/\sigma = 0.5$. The experiments were performed with the presence of the fuselage, hence the isolated curves are most relevant here. The installed figure of merit prediction is very good at low loadings with only a minor overprediction at high loading. The experimental data also included measurement uncertainties slightly over a count in FoM (0.01). Compared to other CFD codes, the installed Helios/OVERFLOW [1]

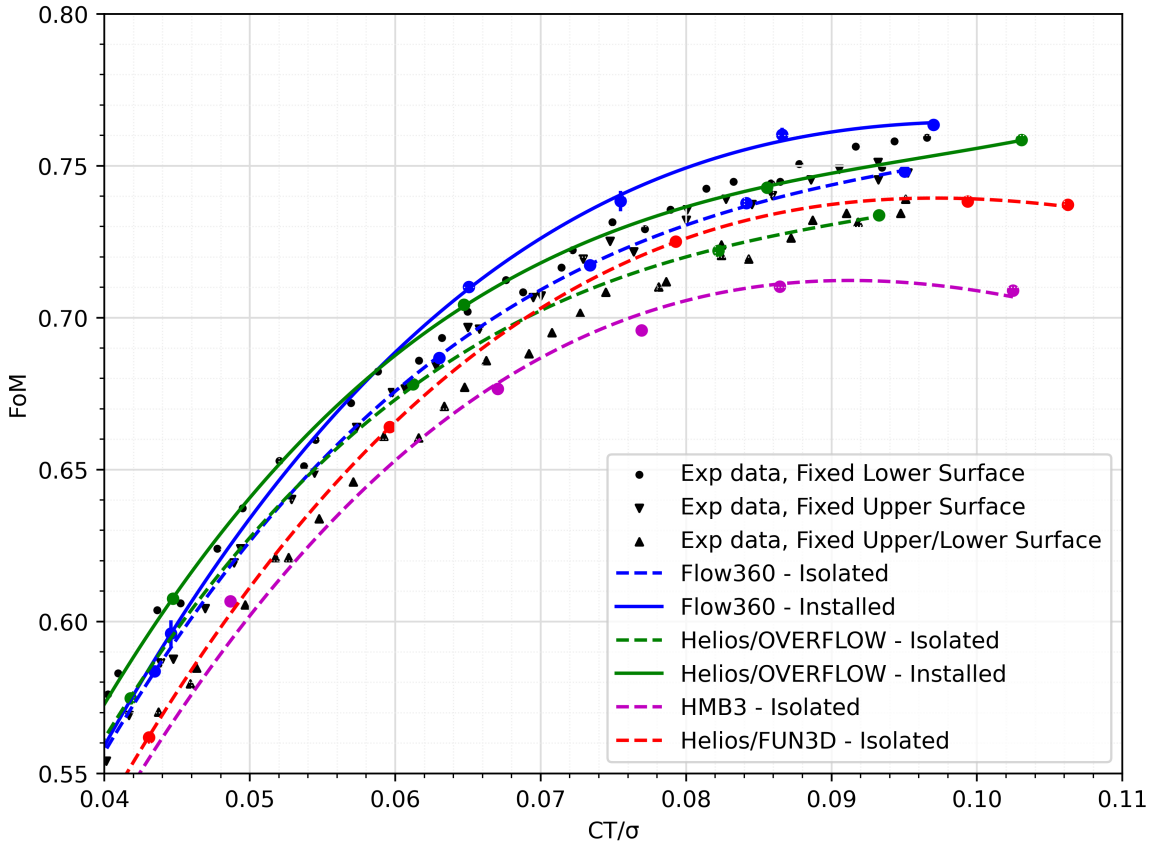

Fig. 18 Hover performance prediction for the isolated and installed HVAB rotor at $M_{tip} = 0.58$ and comparison with experimental data/other CFD codes.

computations are most applicable for comparison, due to the solution fidelity and the inclusion of the fuselage. Here, once again the Flow360 FoM prediction is 1 to 2 counts higher at high thrust though excellent agreement is obtained at low/moderate thrust levels. Noticeably the shape of the curve is also different, with the Flow360 result being closer to the fully-turbulent approximation from Overmeyer [4]. The other CFD codes only obtained isolated rotor results. Here, the Helios/OVERFLOW [1] and Helios/FUN3D [22] show excellent agreement with the Flow360 isolated rotor results, as all three codes are within 2 counts in FoM, despite different coning/lag angles, turbulence models and solver settings. The HMB result stalls earlier than the other codes, showing the necessity for unsteady simulations are high thrust levels. Comparing the isolated and installed Flow360 results, it can be seen that the performance of the rotor increases with the presence of the fuselage. The fuselage induces a beneficial upwash to the rotor, increasing the rotor thrust which leads to a rotor performance improvement. This improvement increases with increasing blade loading. However, as at the same time, the rotor produces a download on the fuselage surface, which leads to a reduction in the overall system thrust. As mentioned previously, slow transients are present in the fuselage loading convergence histories, meaning that long averaging cycles are required for accurate loading predictions. However, the fuselage download values and installed rotor thrust increments are still extracted from the solutions and compared with data from Helios/OVERFLOW [1], shown in Figures 19-20.

The fuselage download predictions show fair agreement with experimental data and Helios/OVERFLOW. At low and high loading the agreement is good, however at moderate loading values the download is over predicted by close to 2%. The experimental data, however, also has a wide range of scatter as indicate by the error bar bounds. Due to the nature of installed rotor calculations, however, this level of accuracy is deemed acceptable with values from longer averaging cycles to be obtained in the future. The installed rotor thrust increment and total system thrust loss show a similar story. Very good agreement is obtained for the installed rotor thrust increase relative to the isolated rotor with a fairly constant offset from the Helios/OVERFLOW results [1]. The total system thrust change shows a similar offset to the Helios/OVERFLOW results as the download prediction.

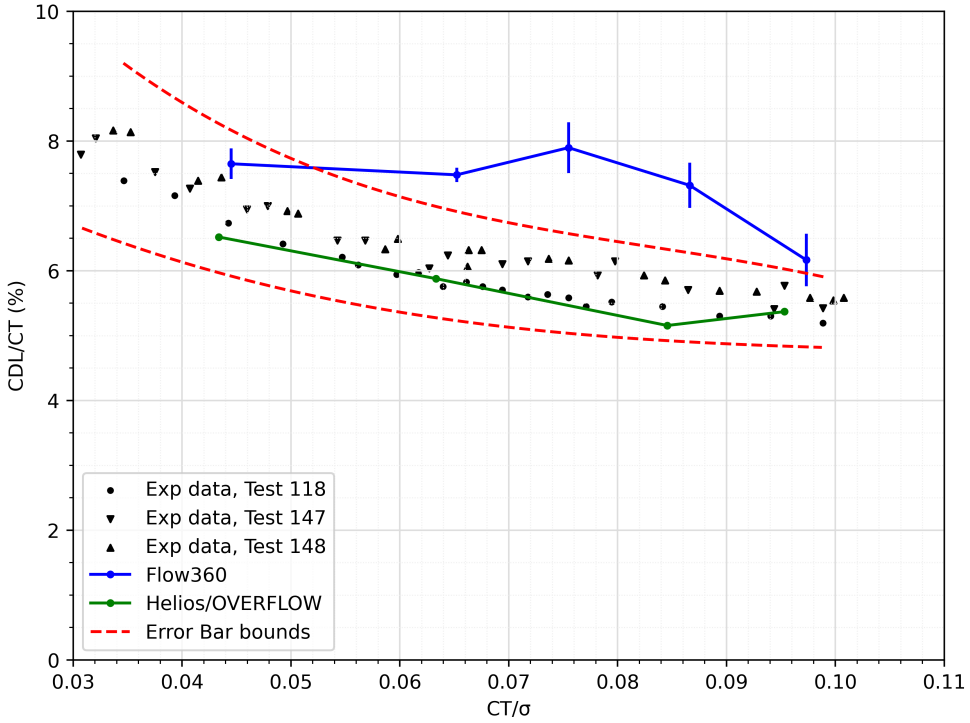

Fig. 19 Fuselage download prediction for the installed HVAB rotor at $M_{tip} = 0.58$.

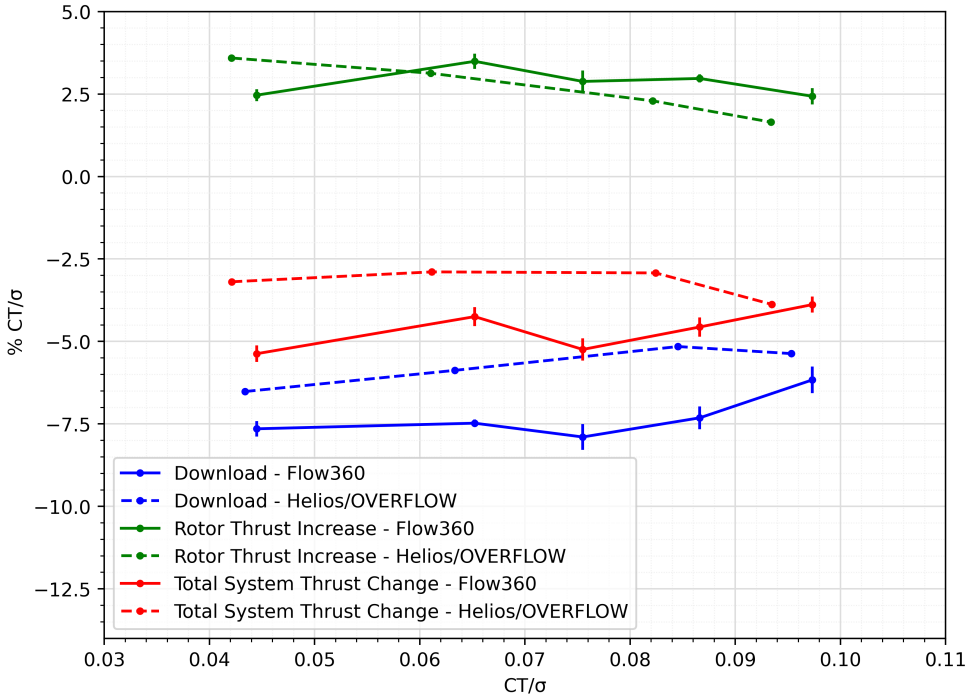

Fig. 20 Installed thrust prediction relative to the isolated rotor for the HVAB rotor at $M_{tip} = 0.58$.

2. HVAB results - $M_{tip} = 0.65$

The HVAB blade results are presented next at a blade tip Mach number of 0.65. The experimental data is not yet officially published, hence only comparisons with other CFD data are made. The data of Helios/OVERFLOW is obtained from [23], whereas the HMB3 data was published in [21].

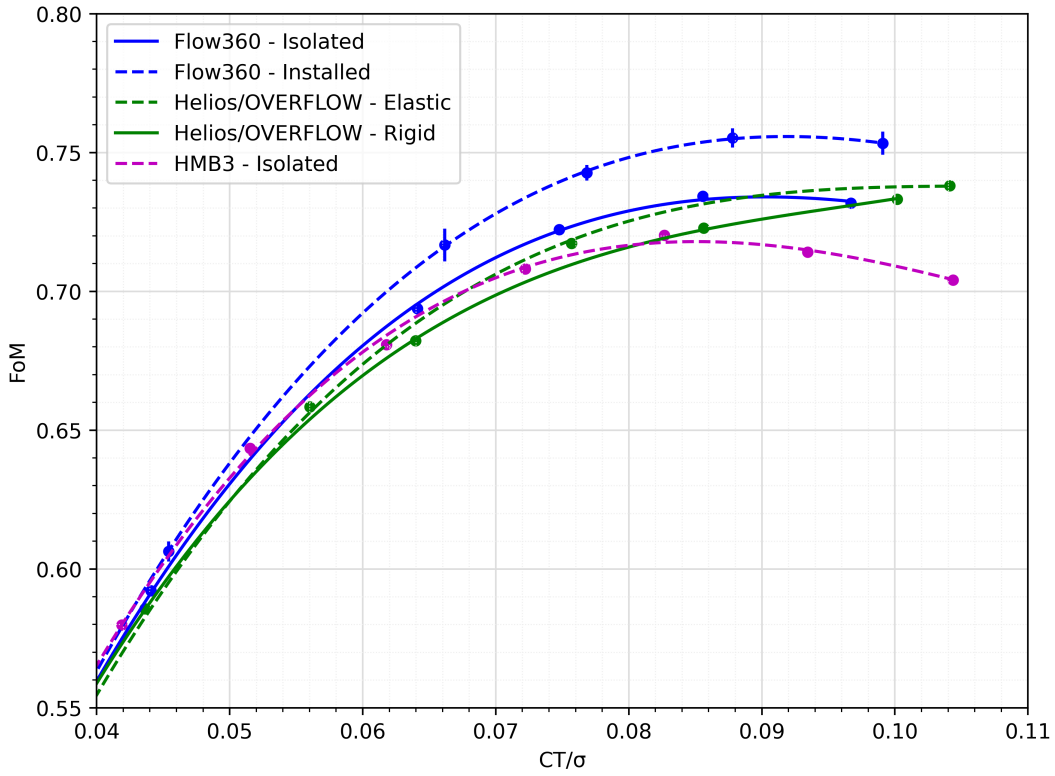

Fig. 21 Hover performance prediction for the isolated and installed HVAB rotor at $M_{tip} = 0.65$ and comparison with other CFD codes.

For the higher blade tip Mach number, $M_{tip} = 0.65$, similar behavior of the code to code differences as in the FoM curves at $M_{tip} = 0.58$. Stronger shock-induced separation, however, is present near the blade tip, hence the performance curves flatten at a lower blade loading. Once again, the Flow360 predictions lead higher FoM values when compared to Helios/OVERFLOW at high blade loading values. There are several possible reasons for this including solver order and levels of dissipation, turbulence modelling and a potential minor sensitivity to lag and cone angles. The Helios/OVERFLOW calculations [23] were performed on grids of over 300 million cells, with 90-100 million nodes used by Flow360. Even for a given number of degrees of freedom, structured codes are known to give higher quality solutions, primarily due often used higher orders of discretization [6]. For example the Helios/OVERFLOW calculations were performed using a sixth order scheme in the near-field and fifth-order scheme in the farfield whilst the Flow360 fluxes are discretized using a 2nd order scheme. Examples of this difference leading to a similar FoM delta between two solvers can be seen in [10] where Helios/OVERFLOW was compared to FUN3D. A similar sensitivity study was also performed in [9], also leading to a slightly higher FoM value for FUN3D than for OVERFLOW/Helios or when using OVERFLOW with a 2nd order scheme. The primary impact of the solution discretization is likely to be the strength of the tip vortices, especially in the first passage, which has a substantial impact on the blade loading. In the current simulations, the first passage tip vortex size at $\theta_{75} = 10^o$ is approximately $r/c_{ref} = 0.27$, whereas Jain [1] reports a value of 0.11-0.12 at the same condition. Another aspect is turbulence modelling, with some studies showing a sensitivity of using SA versus $k - \omega$ SST [24], which is planned as part of future investigations. It is, however, clear that unsteady DES simulations are required for accurate hovering rotor predictions to ensure that the blade does not stall prematurely and that the eddy viscosity ratio levels remain within reasonable values in the rotor wake. It must also be highlighted that engineering accuracy level solutions may not always give the correct answer for the correct reasons. For example, a coarser grid and or time step would lead to improved correlation with Helios/OVERFLOW in

the current study. The fuselage download and installed rotor thrust is examined next, shown in Figure 22, comparing to $M_{tip} = 0.58$ values.

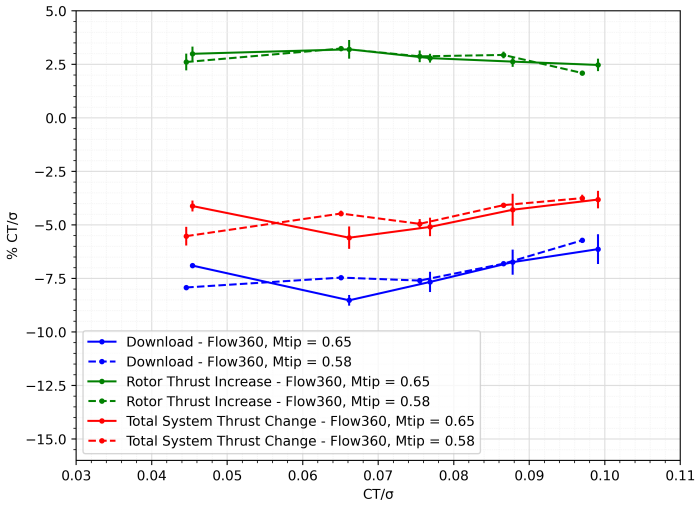

Fig. 22 Installed thrust prediction relative to the isolated rotor for the HVAB rotor at $M_{tip} = 0.65$ and comparison with $M_{tip} = 0.58$ data.

The fuselage download predictions show that percentage values for the fuselage download, rotor thrust increment and total system thrust lost are fairly similar between the two examined blade tip Mach numbers. Generally, the fuselage download value increases leading to a slightly higher total system thrust loss. However, as the values were only extracted from averaging over 5 revolutions, some uncertainty in the predictions is to be expected. The HVAB rotor results are examined further by extracting the sectional loads and surface pressure predictions, shown in Figure 23-24. The surface pressure coefficient values are normalized by local velocity, with the blade collective/coning and lag removed before extracting the data.

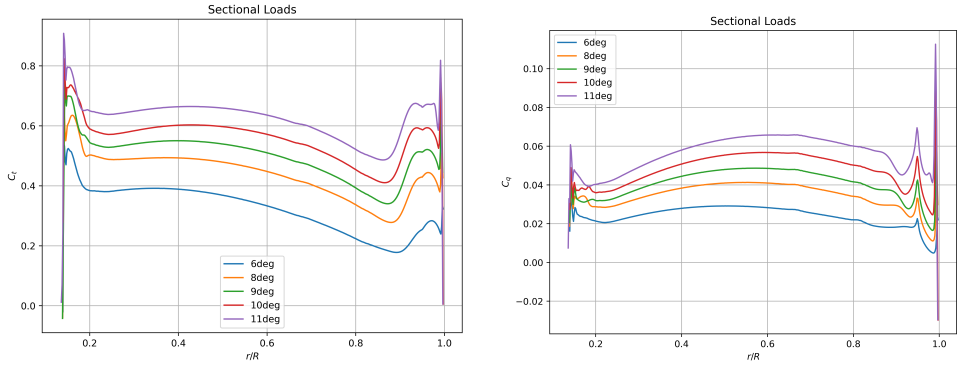

(a) C_t vs θ_{75} (b) C_q vs θ_{75}

Fig. 23 Sectional loads across a range of collectives for the isolated HVAB blade at $M_{tip} = 0.65$.

The sectional loads highlight the impact of tip vortices on the rotor thrust and torque distributions. At a low collective angle, the tip vortices are much weaker, hence the drop in thrust inboard of the tip vortex and increase outboard is much weaker. As the collective angle increases, the effect of the tip vortices becomes much more pronounced. Further inboard, a fairly constant offset per degree an be seen. The surface pressure predictions, show the higher acceleration of the flow on the upper surface at the inboard sections with increasing collective as the suction peak is increased. At the highest collective, a shock appears at r/R=0.9. Further outboard, the surface pressure curves show the presence of shock-induced separation. As the collective is increased, the suction peak stops increasing, with the pressure no longer recovering at 11 degree collective at the most outboard location.

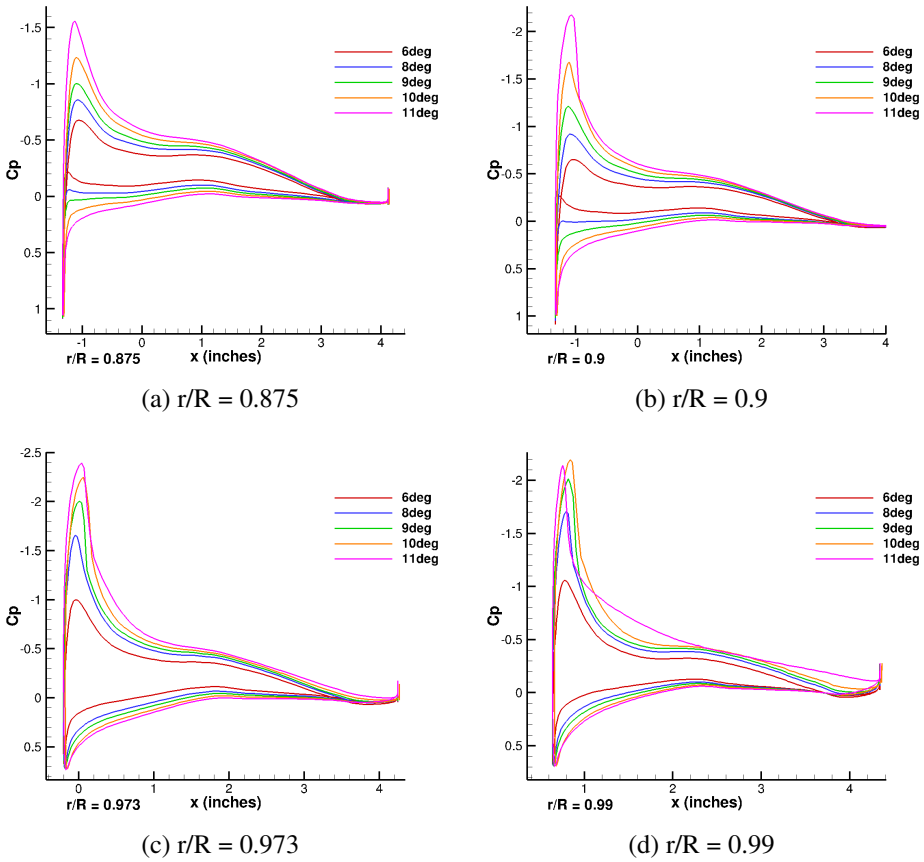

(a) r/R = 0.875 (b) r/R = 0.9

(c) r/R = 0.973 (d) r/R = 0.99

Fig. 24 Surface pressure predictions at four radial stations across a range of collectives for the isolated HVAB blade at $M_{tip} = 0.65$.

To examine the installed calculations further, the instantaneous fuselage surface pressure predictions are extracted from the solutions, shown in Figure 25.

The fuselage surface pressure highlights the increasing fuselage download value with increasing collective. Previously the values were presented as a percentage of installed rotor thrust which also increases with collective angle. The two primary regions, include the forward and aft blade passages. Once again, highly unsteady features can be seen in the root region and lower surface of the fuselage near the ramp. Finally, wake visualizations are also presented at two collective angles shown in Figure 26.

The wake visualizations, highlight the effect of the collective angle on the rotor wake. Firstly, the spacing between the individual rotor tip vortices increases with increasing collective due to the higher thrust produced by the rotor. This can also be seen by the higher Mach number values in the isosurfaces. The low collective wake is also much more coherent than for the high collective case, where secondary flow structures are resolved.

V. Conclusions

This work presented a rigorous mesh sensitivity and time step study for isolated and installed hovering rotor solutions, aiming to assess the level of discretization error sensitivity. Based on the results, a collective sweep was performed with the results compared to available experimental data and other CFD codes. The present work led to the following conclusions:

- For engineering level accuracy isolated rotor solutions, grids of 30 to 40 million nodes are sufficient with a 1 degree time step. Finer time steps are required for installed rotor calculations, especially to accurately capture the fuselage download. Higher resolution solutions do not typically lead to significant benefits in the performance predictions, but lead to much better resolution of the wake, including secondary vortex structures.

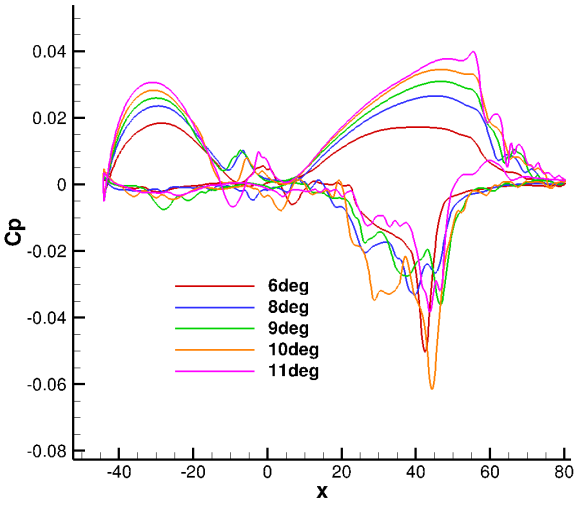

Fig. 25 Instantaneous fuselage surface pressure prediction across a range of collective for the HVAB rotor at $M_{tip} = 0.65$.

- Convergence of installed rotor calculations is significantly more difficult than for isolated rotors due to the presence of slow transients in the solutions, associated with the flow near the root of the blades and unsteady vortex shedding beneath the fuselage. The uncertainties are therefore likely to be higher in the load predictions for the same number of revolutions performed as for an isolated rotor.
- Unsteady DES-based simulations are required for accurate hover performance predictions especially at high blade loading. This prevents pre-mature stall typically seen in steady hovering rotor solutions and the build-up of turbulent eddy viscosity in the rotor wake.
- The Flow360 hover performance predictions are within 1 count in FoM to reference experimental data and 1 to 2 counts to other CFD codes, with the FoM values showing a consistent upper limit offset from other data sets. This will be investigated as part of future work, focusing on turbulence modelling, lag/cone angle and even finer near-wake resolution sensitivities.
- The fuselage download predictions are within 2% to reference data, with further investigations planned on the number of revolutions required to obtain good statistical convergence.

References

[1] Jain, R., *CFD Performance and Turbulence Transition Predictions of an Installed Model-scale Rotor in Hover*, AIAA Scitech Forum, 55th Aerospace Sciences Meeting, Grapevine, TX, 2017.

[2] Chaderijan, N., *Advances in Rotor Performance and Turbulent Wake Simulation using DES and Adaptive Mesh Refinement*, Seventh International Conefereces on Computational Fluid Dynamics (ICCFD7), Hawaii, USA, 2012.

[3] Barakos, G. N., and Jimenez-Garcia, A., *Hover Predictions of the S-76 Rotor using HMB2 - Model to full Scale*, San Diego, CA, 2016.

[4] Overmeyer, A., and Martin, P., *Measured Boundary Layer Transition and Rotor Hover Performance at Model Scale*, AIAA Scitech Forum, 55th Aerospace Sciences Meeting, Grapevine, TX, 2017.

[5] Hover Prediction Workshop Steering Committee, "AIAA Rotorcraft Hover Prediction Workshop (HPW)," , 2022. URL `https://www.aiaa-hpw.org`.

[6] Egolf, T., Hariharan, N., Narducci, R., and Reed, E., *AIAA Standardized Hover Simulation: Hover Performance Prediction Status and Outstanding Issues*, AIAA Scitech Forum, 55th Aerospace Sciences Meeting, Grapevine, TX, 2017.

[7] Jain, R., *Effect of Facility Walls and Blade Aeroelasticity on the PSP Rotor Hover Performance Predicitons*, AIAA Scitech Forum, 56th Aerospace Sciences Meeting, Kissimee, FL, 2018.

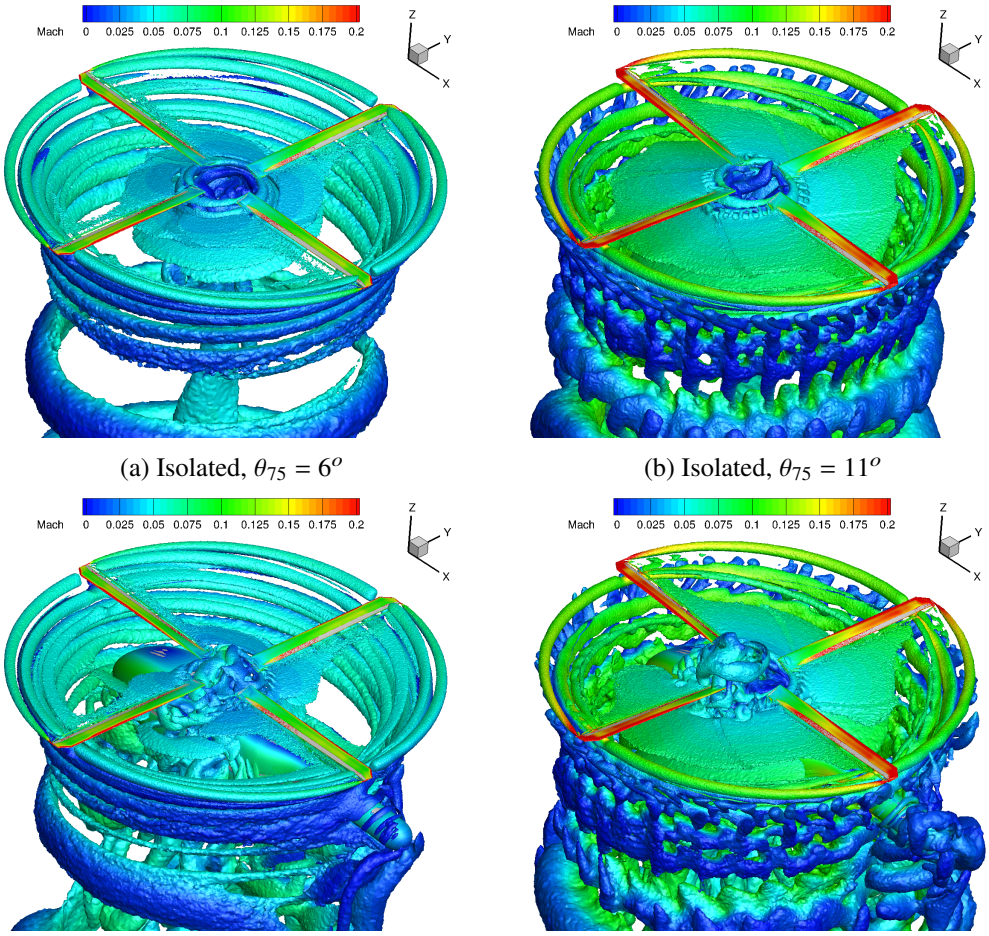

(a) Isolated, $\theta_{75} = 6^o$ (b) Isolated, $\theta_{75} = 11^o$

(c) Installed, $\theta_{75} = 6^o$ (b) Installed, $\theta_{75} = 11^o$

Fig. 26 Wake visualization using Q-criterion (2e-06) with at two collectives for the isolated and installed HVAB rotor at $M_{tip} = 0.65$.

[8] Hover Prediction Workshop Steering Committee, "Hover Focus Problem," , 2022. URL `https://www.aiaa-hpw.org/real-hover-problem`.

[9] Jain, R., "Sensitivity Study of High-Fidelity Hover Predictions on the Sikorsky S-76 Rotor," *Journal of Aircraft*, Vol. 55, No. 1, 2018, pp. 78–88. https://doi.org/10.2514/1.C034076.

[10] Abras, J., and Hariharan, N., "Comparison of Computational Fluid Dynamics Hover Predictions on the S-76 Rotor," *Journal of Aircraft*, Vol. 55, No. 1, 2018, pp. 12–22. https://doi.org/10.2514/1.C034121.

[11] Hover Prediction Workshop Steering Committee, "File Share - HVAB Geometry," , 2022. URL https://www.aiaa-hpw.org/file-share.

[12] Hover Prediction Workshop Steering Committee, "HVAB Rotor Test Case," , 2022. URL https://www.aiaa-hpw.org/hvab-rotor.

[13] Jain, R., *Hover Predictions for the S-76 Rotor with Tip Shape Variation using CREATE-AV Helios*, AIAA Scitech Forum, 53rd Aerospace Sciences Meeting, Kissimmee, FL, 2015.

[14] Schaeffler, N., Allan, B., Lienard, C., and Le Pape, A., *Progress Towards Fuselage Drag Reduction via Active Flow Control: A Combined CFD and Experimental Effort*, 36th European Rotocraft Forum, Paris, France, 2010.

[15] Haimes, R., and Dannenhoffer, J., *The Engineering Sketch Pad: A Solid-Modeling, Feature-Based, Web-Enabled System for Building Parametric Geometry*, 2st AIAA Computational Fluid Dynamics Conference, 2013.

[16] Yoon, S., Chaderijan, N., Puliam, T., and Holst, T., *Effect of Turbulence Modeling on Hovering Rotor Flows*, AIAA Aviation, 45th AIAA Fluid Dynamics Conference, Dallas, TX, 2015.

[17] Potsdam, M., and Puliam, T., *Turbulence Modeling Treatment for Rotorcraft Wakes*, American Helicopter Society Specialist's Conference on Aeromechanics, San Francisco, CA, 2008.

[18] Narducci, R., *Hover Performance Assessment of Several Tip Shapes using OVERFLOW*, AIAA Scitech Forum, 53rd Aerospace Sciences Meeting, Kissimmee, FL, 2015.

[19] Cadence, "Pointiwse V18.6R1," , 2022. URL https://www.pointwise.com/index.html.

[20] Abras, J., Narducci, R., and Hariharan, N., *Wake Breakdown of High-fidelity Simulations of a Rotor in Hover*, AIAA Scitech 2019 Forum, San Diego, CA, 2019.

[21] Jimenez-Garcia, A., and Barakos, G., *Numerical Simulations on the PSP Rotor Using HMB3*, AIAA Scitech Forum, SciTech 2018, Kissimmee, FL, 2018.

[22] Wong, T., *Application of CREATE TM -AV Helios in an Engineering Environment: Hover Prediction Assessment*, AIAA Scitech Forum, 55th Aerospace Sciences Meeting, Grapevine, TX, 2017.

[23] Jain, R., *CFD Hover Performance and Transition Predictions on the PSP and HVAB Rotors using CREATE TM -AV Helios*, AIAA Scitech Forum, SciTech 2022, San Diego, CA, 2022.

[24] Yoon, S., Puliam, T., and Chaderijan, N., *Simulations of XV-15 Rotor Flows in Hover Using OVERFLOW*, Fifth Decennial AHS Aeromechanics Specialists' Conference, San Francisco, CA, 2014.